
ELSEVIER

Nuclear Instruments and Methods in Physics Research B 171 (2000) 81–95

NIM B
Beam Interactions with Materials & Atoms

www.elsevier.nl/locate/nimb

Low-energy positron scattering from atoms and molecules using positron accumulation techniques

S.J. Gilbert [a,*], J. Sullivan [a], R.G. Greaves [b], C.M. Surko [a]

[a] *Department of Physics, University of California, San Diego, 9500 Gilman Drive, La Jolla, CA 92093-0319, USA*
[b] *First Point Scientific, Inc., Agoura Hills, CA 91301, USA*

Received 18 November 1999; received in revised form 2 February 2000

Abstract

Positron scattering from atoms and molecules is studied at low values of incident positron energy. The experiments use a cold magnetized positron beam formed in a positron accumulator. A discussion of positron scattering in a magnetic field is presented along with differential cross-sections (DCS) for positron–atom collisions and positron–molecule total vibrational excitation cross-sections. Absolute values of the DCS for elastic scattering from argon and krypton are measured at energies ranging from 0.4 to 2.0 eV. The first low-energy positron–molecule vibrational excitation cross-sections have been measured (i.e., for carbon tetrafluoride at energies ranging from 0.2 to 1 eV). Using information gained from these experiments a second generation scattering apparatus is described, which was designed and built specifically for scattering experiments using a magnetized positron beam. This apparatus has a number of improvements, including an order of magnitude higher throughput, better energy separation between elastic and inelastic scattering events, and improved measurement of the absolute pressure of the test-gases. Analysis techniques for the data taken in these experiments using a retarding potential energy analyzer and possible extensions of these experiments are also discussed.

PACS: 34.85.+x; 41.75.Fr; 34.50.-s; 34.50.Ez
Keywords: Cross-section; Vibrational; Scattering; Beam; Positrons; Monoenergetic

1. Introduction

The interaction of antimatter with matter is an interesting and active field of study [1–13]. One of the simplest of these types of interactions is between a positron and an atom or molecule. Such interactions are important in atomic physics [1–9] and surface science [10,14], and they have potential technical applications such as mass spectrometry [12,13]. Although some aspects of these interactions have been studied in detail [1,6,9,15], most positron-scattering experiments to date have concentrated on beam energies greater than 1 eV due to technical restrictions. For example, before the work described here, the lowest energy positron

* Corresponding author. Tel.: +1-858-534-6569; fax: +1-858-534-6574.
E-mail address: sjgilbert@ucsd.edu (S.J. Gilbert).

0168-583X/00/$ - see front matter
PII: S0168-583X(00)00056-2

differential cross-section $d\sigma/d\Omega$ (DCS) measurements were of argon at 2.2 eV [16], and the only known positron total vibrational excitation cross-sections were for CO_2 at energies above 3 eV [5]. The only exceptions to this are some total cross-sections which have been measured at energies below 1 eV [1–3]. There are, however, many interesting questions at low values of positron energy, including the existence of positron bound states in atoms or molecules, the role of vibrational excitation in the formation of long lived positron–molecule resonances [7,8], and the understanding of large-molecule fragmentation by positrons [12,13].

The main reason for the lack of scattering measurements below 1 eV is the difficulty in producing cold positron beams. This paper will not discuss the many elegant, high-resolution *electron* scattering experiments that have been carried out to date; see for instance [17–19]. It is important to point out, however, that the techniques used to form cold electron beams are not applicable for positrons. Typically, electron beams with small energy spreads (~25 meV) are formed by collimation and energy selection of a copious source of electrons, and similar sources for positrons are not available. Electron–atom and electron–molecule scattering experiments at even higher-energy resolutions have been performed. For example, by using a laser with an energy slightly above the photo-ionization threshold of argon, cold (<1 meV) electrons can be produced, which are then used to scatter from the test-gas [20]. However, even with such sources of cold electrons, low-energy electron scattering experiments are still difficult. To our knowledge the lowest electron–argon DCS measurements are at 1 eV [21].

To form a cold positron beam, the limited supply of positrons must be used efficiently. Typically, positrons for a slow beam originate either from a radioactive source or from a particle accelerator. In both cases, the positrons must be slowed from initial energies of several hundred keV to a few eV before beam formation is possible. This is most efficiently accomplished using a solid-state moderating material [10,11,22–24]. Moderated beams have energies of a few electron volts and an energy spread of 0.3–5 eV, depending on the moderating material used. Until now, most positron-scattering experiments have used these moderated beams as a cold positron source, limiting the experiments to energies greater than about 1 eV [1–5,9].

We have been able to overcome these limitations to achieve a high intensity, cold, magnetized positron beam (i.e., 18 meV parallel energy spread) [25,26]. Using the cold beam we were able to make new kinds of positron-scattering measurements. These include measuring positron–argon and positron–krypton DCS at energies lower than any previous measurements (0.7–2.0 eV), and making the first low-energy measurement of positron–molecule total vibrational cross-sections at energies as low as 0.2 eV, studying the ν_3 excitation of CF_4 [27].

Besides some total cross-section measurements [1–3], positron-scattering experiments have been traditionally carried out using moderated positrons in an *electrostatic* beam. The positrons are focused onto a highly compact target such as a gas jet, which precisely defines the scattering angle. Typically, a channeltron detector with a retarding potential grid in front of it is placed on a movable arm to measure the DCS [21]. Our beam is created from a reservoir of cold positrons, confined in a Penning trap in a 0.15 T magnetic field. Because the cold positron beam is formed in a magnetic field, it is expedient for us to also conduct the positron-scattering experiments in a field of comparable magnitude. This led us to combine existing techniques and develop new ones in order to perform measurements such as elastic DCS, total inelastic cross-section, and total cross-sections for positrons scattering in a magnetic field.

Many of the techniques described here have been used elsewhere in one form or another. For example, positron–atom total cross-sections are typically measured using a gas cell and a positron beam which is guided through the cell by a weak magnetic field [1–3]. Retarding potential analyzer (RPA) measurements have been used previously in conjunction with a spatially varying magnetic field to characterize the energy distributions of moderated positrons [24]. Positron–atom DCS have been measured in a magnetic field using time-of-flight methods [16]. Magnetized pulsed beams have been

created using a non-thermal reservoir of positrons [28–30]. In addition to combining these techniques, the new features of the work described here are the ability to resolve inelastic from elastic scattering events using a varying magnetic field between the scattering and analysis regions (see Section 5.2), and the use of an N_2 buffer gas and three-stage Penning trap to form a cold pulsed or continuous beam [25,26,31]. By combining the cold positron beam formed in this manner with methods to perform scattering experiments in a magnetic field, we have been able to extend the limits of positron–atom and positron–molecule scattering experiments into a new range of low positron energies.

Using the information gained from initial experiments, a new scattering experiment has been constructed and is now being brought into operation. Along with this new scattering apparatus, we have recently completed construction of a new positron accumulator [32]. The combination of the new accumulator and this scattering apparatus is expected to offer even further improvements in the capability to study low-energy positron physics, including a brighter positron beam and 10 times higher throughput by eliminating the need to repetitively pump out the test-gas while trapping positrons. The new apparatus also has the capability to operate at a magnetic field ratio four times greater than that previously possible, and this provides correspondingly greater discrimination for inelastic scattering studies. All of these improvements lead to either increased signal-to-noise ratio or improved energy resolution. The initial results from the new apparatus are very promising. We believe that the studies described here are the beginning of a broad experimental program in low energy positron atomic physics.

This paper is organized in the following manner. The dynamics of positron motion in a magnetic field are discussed, since this is central to the scattering techniques used in the experiments described here. The techniques used for positron accumulation and cold beam formation are reviewed. Then scattering from atoms and molecules in a magnetic field is described, followed by a discussion of the methods used to measure differential elastic, inelastic and total cross-sections. Measurements of elastic positron DCS on argon and krypton, and inelastic vibrational cross-sections for CF_4, are then summarized. The paper continues with a discussion of other effects relevant to this kind of measurement, and concludes with a set of remarks emphasizing the future of experiments in this area of low-energy positron atomic physics.

2. Charged particle motion in a magnetic field

Because our positron-scattering experiments are conducted in a magnetic field, it is helpful to briefly review charged particle motion in such a field. Fig. 1 shows a positron's path in a magnetic field. The positron follows a helical orbit which can be conveniently split into two distinct motions, a linear motion along the magnetic field and a circular motion in the direction perpendicular to the field. The radius of this orbit, known as the cyclotron radius r_c, is proportional to the particle's velocity and inversely proportional to the magnetic field strength. Specifically, $r_c = mv_\perp/eB$, where m is the charged particle mass, $v_\perp$ the particle's velocity perpendicular to the magnetic field, e the charge, and B is the magnetic field strength. A typical positron in the cold beam will have $v_\perp \sim \sqrt{2kT/m}$, where kT is the thermal energy of the room temperature positrons (≈ 0.025 eV) [see Section 3]. The cyclotron radius of such a positron when placed in a 0.1 T field will therefore be $r_c \sim 5$ μm, which has been greatly exaggerated in Fig. 1 to show the helical motion.

It is convenient to split the total particle kinetic energy into the components due to these two motions. We express the positron total energy, E, as $E = E_\perp + E_\parallel$, where $E_\parallel$ is the kinetic energy

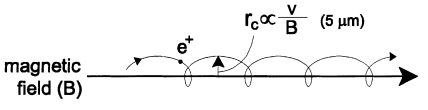

Fig. 1. Charged particle motion in a magnetic field. The helical path can be separated into a circular motion in the plane perpendicular to the field and a linear motion along the field. The total kinetic energy, E, of the particle is the sum of the kinetic energy associated with motion along the field, $E_\parallel$, and the kinetic energy due to the circular motion, $E_\perp$, where $E = E_\perp + E_\parallel$.

along the magnetic field and $E_\perp$ is the kinetic energy in the circular motion perpendicular to the magnetic field. We use a retarding potential analyzer (RPA) to determine the energy distribution in the positron beam. In the magnetic field, the RPA only affects the particle's parallel kinetic energy, and it therefore only measures $E_\parallel$.

3. Positron trapping and cold beam formation

The experimental setup for the scattering apparatus is shown schematically in Fig. 2(a). High-energy positrons from a 90 mCi ^{22}Na source are moderated to about 1.5 eV using a solid neon moderator (not shown) [23]. The moderated positrons are trapped in our newly designed positron accumulator [32] at a rate of 1×10^6 positrons per second by a series of inelastic collisions with a nitrogen buffer gas [31,33]. The trapped positrons are confined radially by a 0.15 T magnetic field and axially by an electrostatic potential well created by the accumulator electrodes (see Fig. 2(b)). Once the positrons are trapped, they cool to room temperature (0.025 eV) in approximately 1 s by further collisions with the nitrogen buffer gas [33].

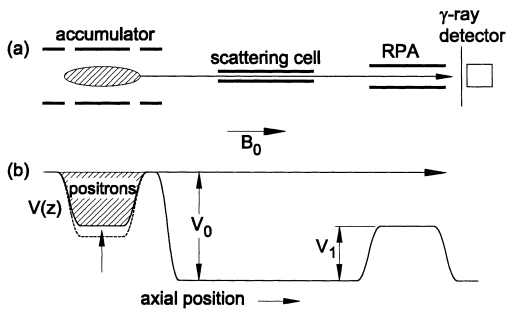

Fig. 2. (a) Schematic diagram of the scattering experiment showing the arrangement of the positron plasma and beam, the scattering cell, and retarding potential analyzer (RPA). (b) Plot of the potential profile $V(z)$ used in a scattering experiment. As the depth of the potential well of the positron accumulator is reduced, positrons are forced over the potential barrier creating a positron beam at energy eV_0 which interacts with a test-gas in the scattering cell. The parallel energy distribution of the transmitted beam is measured using the retarding voltage V_1 of the RPA.

After a positron plasma has been accumulated and cooled, a positron beam is generated by decreasing the depth of the potential well confining the positrons, which ejects a fraction of the stored positrons. During this process, the entrance gate electrode is placed 1 V higher than exit gate electrode (the left and right electrodes of the accumulator in Fig. 2, respectively) to ensure that the positrons leave the accumulator via the exit gate. The energy of the positron beam (eV_0) is set by the potential of the exit gate electrode and can be adjusted from tenths of an electron volt up to a hundred eV without any increase in beam energy spread. In order to achieve a narrow energy spread in both the parallel and perpendicular components, care must be taken in the beam formation procedure. The main contributing factor to the parallel energy spread is the amount of space charge in the beam. By using only a small number of positrons ($\sim 2 \times 10^5$) at a time to form a beam, we have been able to achieve parallel beam energy spreads as small as 0.018 eV, which is colder than the stored positron's temperature ($kT \approx 0.025$ eV). We have shown previously that the perpendicular energy spread of the beam, which is determined by the stored positron's temperature, is unaffected by the beam formation, i.e. $E_\perp \approx 0.025$ eV [33].

In order to independently measure the positron beam's parallel energy spread and total energy an RPA is used. The positrons are magnetically guided through the cylindrical RPA and detected using a 3-inch NaI(Tl) γ-ray detector (see Fig. 2). By measuring the number of positrons that pass through the RPA as a function of the applied potential, E_1, the parallel beam energy distribution can be determined. The energy distribution of a typical positron beam is shown in Fig. 3. The filled circles are the measured data. For applied voltages less than the beam energy (in this case 1.7 eV) all of the positrons pass through the RPA and are detected. When the applied voltage is above the beam energy none of the positrons are transmitted through the RPA. As the applied voltage on the RPA scans through the beam energy from low to high, the coldest positrons get cut off first, and finally all of the positrons are cut off. The dotted line in Fig. 3 is a fit to the data, and the solid line is

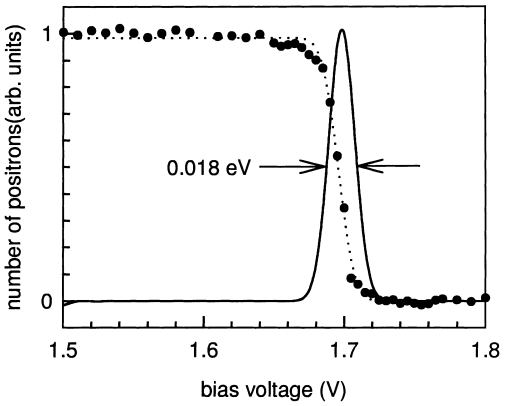

Fig. 3. Retarding potential energy analyzer data showing the parallel energy distribution of a typical positron beam. Filled circles are measured data, and the dotted line is an error function fit. The solid line, representing the parallel energy distribution of the beam, is the derivative of the fit.

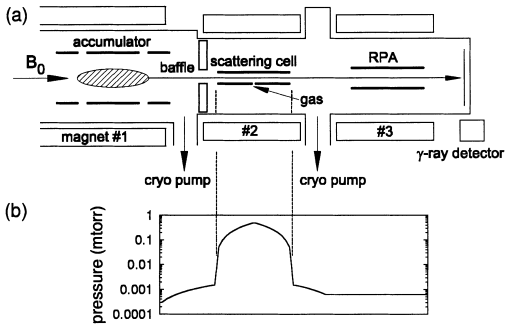

Fig. 4. (a) Schematic diagram of the scattering apparatus and vacuum system used to isolate the test-gas from the nitrogen buffer gas. The test-gas is introduced at the center of the scattering cell and is pumped out at both ends by two cryopumps. A baffle is placed between the positron accumulator and the scattering cell to further improve the isolation. (b) Calculated test-gas pressure profile along the axis of the scattering apparatus. The gas pressure near the ends of the scattering cell is more than two orders of magnitude smaller than at the center.

the derivative of the fit showing the FWHM of 0.018 eV.

4. Scattering experiments using a magnetized positron beam

The scattering experiments are conducted in the following manner. First, positrons are accumulated for ~0.1 s and then cooled to room temperature in ~1 s. A cold beam of approximately 10^5 positrons is formed using the technique described above. It is guided magnetically through the scattering cell where it interacts with the test-gas. A schematic diagram of the scattering experiment, showing the vacuum and pumping scheme used to form an isolated region of test-gas in the scattering cell, is displayed in Fig. 4(a). Test-gas is continually introduced into the center of the scattering cell, which is 38 cm long with a 1 cm internal diameter, and pumped out at both ends using two cryo-pumps (see Fig. 4(a)). A well localized region of higher pressure is created through differential pumping between the 1 cm diameter scattering cell and the 9 cm diameter vacuum chamber. Fig. 4(b) shows the calculated pressure profile of the test-gas in the scattering apparatus. A typical gas pressure of 0.5 mTorr in the center of the gas cell is reduced by over two orders of magnitude by the ends of the cell. This permits operation of the experiment in steady-state with the test-gas isolated in the scattering cell and the nitrogen buffer gas confined to the accumulator. In our previous scattering apparatus it was necessary to pump out the nitrogen buffer gas before the test-gas could be introduced. By eliminating this complication we have been able to increase our throughput by an order of magnitude.

To further reduce the effects of the test-gas on the accumulator fill cycle, a 1.2 cm diameter gas baffle was placed between the scattering cell and accumulator (see Fig. 4). In order to reduce the effects of multiple scattering, the test-gas pressure in the scattering cell is adjusted so that 10% of the positron beam is scattered by the gas. We are able to determine the average absolute pressure through the scattering cell in a gas-independent manner, with better than 1% absolute accuracy. This is accomplished with a thermally regulated capacitance manometer gauge used to directly measure the pressure at the center of the scattering cell. We verify that the operating pressures used in the scattering cell (typically 0.1–1 mTorr) are in a pressure regime where the measured scattering cross-sections are independent of the test-gas pressure. The scattered beam exits the cell and is

energy analyzed by the RPA. In order to improve the statistics, the entire 2 s sequence is typically repeated 1000 times, and so a typical data run takes 11 h to complete.

5. Beam energy analysis

The scattering measurements presented here exploit the behavior of positrons in a 0.1 T magnetic field. As mentioned earlier the total positron energy, E, can be expressed as $E = E_\perp + E_\parallel$, where $E_\perp$ and $E_\parallel$ are the contributions to the motion perpendicular and parallel to the magnetic field, respectively. Fig. 5 depicts a positron scattering from an atom or molecule in a magnetic field. The positron follows a helical path along the magnetic field with a small (5 μm) cyclotron orbit. Upon colliding with a test-gas atom the positron scatters at an angle θ, transferring some of its kinetic energy, which is initially in the parallel component, $E_\parallel$, into the perpendicular component, $E_\perp$. The interaction occurs on an atomic length scale (i.e., $b \sim 1$ Å). Since b is orders of magnitude smaller than the motion caused by the magnetic field, the positron scatters as if it were in a field-free region. After the scattering event, the positron continues to travel along the magnetic field with some of its total energy E transferred to the test atom and some into $E_\perp$ depending on the angle scattered and

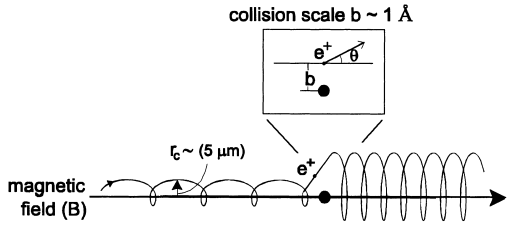

Fig. 5. Positron scattering in a magnetic field. A positron from a cold beam, with most of its kinetic energy in the parallel component, $E_\parallel$, follows magnetic field until it scatters from an atom (see inset). The scattering event transfers some total energy, E, of the positron from $E_\parallel$ into $E_\perp$, depending on the scattering angle and atomic processes involved. The scattered positron continues along the field with an increased value of $E_\perp$ and decreased $E_\parallel$.

the elastic or inelastic nature of the scattering event.

5.1. Elastic DCS analysis

In cases where only elastic scattering is present (i.e. noble gases below the threshold for electronic excitation and positronium formation), we can extract the DCS from the parallel energy distribution of the scattered beam. Fig. 6 shows a calculated energy distribution in ($E_\perp$, $E_\parallel$) space for a cold 1 eV beam (a) before, and (b) after an elastic scattering event. Because the collision is elastic, the total positron energy E is conserved (Fig. 6(b) dashed line); therefore the scattering angle θ is determined solely by the amount of energy transferred from $E_\parallel$ to $E_\perp$. If we assume that the initial trajectory of the positron is in the direction of the magnetic field, then after an elastic scattering event, the positron velocity, $v_\parallel$ in the direction of the field will be $v_\parallel = v\cos(\theta)$, where v is the positron's total velocity, $v_\parallel$ the velocity along the magnetic field, and θ is the scattering angle. Thus, $E_\parallel = E\cos^2(\theta)$, which can be rewritten as

$$\theta = \cos^{-1}\sqrt{E_\parallel/E}. \tag{1}$$

The assumption that the incoming positron's trajectory is in the direction of the magnetic field is valid for $E_\parallel \gg E_\perp$. Typically a positron will have $E_\parallel \sim 1$ eV and $E_\perp \sim 0.025$ eV. This means that the positrons have an initial angular spread $[\Delta\theta = \sin^{-1}(v_\perp/v)]$ of $\sim 9°$, which provides an estimate of our angular resolution.

In order to calculate the DCS, we need to know not only to which angle a given $E_\parallel$ corresponds, but also how many positrons are scattered into that angle. For a given applied voltage V_0, the RPA discriminates against all particles with parallel energy components $E_\parallel$ less than eV_0, and so the RPA measures the parallel energy distribution integrated over energies above $E_\parallel$. Therefore the integrated parallel energy distribution normalized to unity $I(E_\parallel)$ measures the probability for a positron to have a parallel energy greater than or equal to $E_\parallel$. Using this integrated energy distribution, the elastic DCS is obtained by

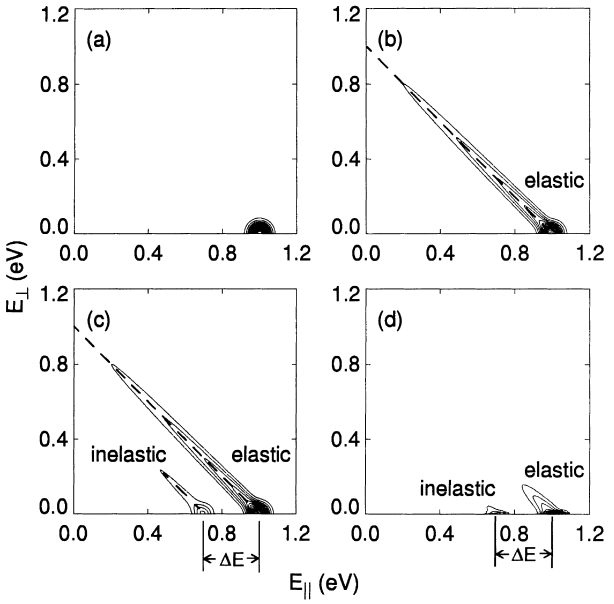

Fig. 6. Simulated effects of elastic and inelastic scattering on the parallel and perpendicular energy components of an initially strongly magnetized, cold charged particle beam: (a) incident 1 eV beam; (b) the effect of elastic scattering; (c) both elastic and inelastic scattering; (d) the scattered beam shown in (c), following an adiabatic reduction of the magnetic field by a factor of $M = 10$. The dashed lines show the conservation of total energy as the positrons scatter through angle θ. The total energy loss from the inelastic collision is indicated by the shift ΔE.

$$\frac{d\sigma}{d\Omega} = C\left(\frac{dE_{\parallel}}{d\Omega}\right)\left(\frac{dI(E_{\parallel})}{dE_{\parallel}}\right), \tag{2}$$

where the constant of proportionality, C, relates the scattering cross-section to the scattering probability, $dE_{\parallel}/d\Omega$ represents the relation between the effective solid angle sampled and the energy increments used in the RPA measurement, and $dI(E_{\parallel})/dE_{\parallel}$ is the probability that a positron will be scattered into the energy range $dE_{\parallel}$. The constant C is given by

$$C = \frac{\sigma}{P_s} = \frac{1}{nl}, \tag{3}$$

where σ is the cross-section, P_s the probability of a scattering event, n the number density of the test-gas molecules, and l is the positron path length through the scattering cell. For the experiment described here,

$$C(a_0^2) = 0.029/P_{av}\ (\text{Torr}), \tag{4}$$

where P_{av} is the average pressure. We have assumed a scattering cell temperature of 27°C and a path length equal to the scattering cell length of 37 cm. The quantity $dE_{\parallel}/d\Omega$ in Eq. (2) can be calculated using Eq. (1) to yield

$$\frac{dE_{\parallel}}{d\Omega} = -\frac{1}{\pi}\sqrt{EE_{\parallel}}. \tag{5}$$

Substituting Eq. (5) into Eq. (2), we obtain a final relationship between the RPA data $I(E_{\parallel})$ and the DCS for the elastic scattering event

$$\frac{d\sigma}{d\Omega} = C'\sqrt{EE_{\parallel}}\left(\frac{dI(E_{\parallel})}{dE_{\parallel}}\right), \tag{6}$$

where $C' = -C/\pi$. Using Eqs. (1) and (6) we can determine the DCS for a positron–atom or positron–molecule elastic scattering event from the parallel energy distribution of the scattered beam.

5.2. Measurement of total inelastic cross-sections

We are also able to measure total inelastic cross-sections for positron–atom or positron–molecule scattering. Fig. 6(c) shows the simulated

effects on $E_\perp$ and $E_\parallel$ of both elastic and inelastic scattering on a positron beam. The positrons that participate in an inelastic scattering event lose some energy ΔE, transferring it to the atom or molecule, and are represented by the shifted beam in Fig. 6(c). In order to measure the total inelastic cross-section, we must be able to distinguish between an inelastically scattered positron that has lost ΔE to the target atom and an elastically scattered positron whose scattering angle corresponds to a loss of ΔE in its parallel energy component. It is clear from Fig. 6(c) that by simply measuring the parallel energy distribution of the scattered beam we cannot distinguish between these two events. To circumvent this problem, we take advantage of the adiabatic invariant, $E_\perp/B$, for a charged particle in a slowly varying magnetic field of strength B. If the positron scatters in a magnetic field B_s and is guided adiabatically into a lower field B_a, where it is analyzed (see Fig. 4 magnets #2 and #3, respectively), then $E_\perp$ is reduced by the ratio of the large field to the small field, $M = B_s/B_a$, while the total energy of the positron is still conserved. For a large reduction in the field ($M \gg 1$), the resulting parallel energy $E_\parallel$ is approximately equal to the total energy E. Fig. 6(d) shows the scattered beam after it has undergone a reduction $M = 10$ in magnetic field. It is clear from this figure that the parallel energy distributions of the elastic and inelastic scattering events are now well separated, and therefore they can be discriminated by the RPA.

5.3. Total cross-sections

Although we have not yet published any data on positron total scattering cross-sections, such measurements are done routinely using magnetized positron beams [1–3] and are, in principle, easy to do with the system described above. The probability for a positron to undergo any scattering event (which is proportional to the total scattering probability) can be measured in two steps. First the RPA is set to 0 V, and the total beam strength is measured. Then the unscattered beam strength is measured by adjusting the RPA voltage a small increment, ΔV, below the beam energy. The analyzer rejects all positrons which have either undergone an inelastic scatter with energy loss greater than $e\Delta V$ or have transferred parallel energy greater than $e\Delta V$ into perpendicular energy by elastic scattering, thus discriminating against all scattered positrons. The total scattering cross-section is determined by comparing this signal to the total beam strength and scaling it by the constant of proportionality C, derived in Eq. (4), which relates the TCS to the scattering probability. By repeating this at different values of beam energy, the total cross-section as a function of beam energy can be determined for a given atomic or molecular species.

6. Experimental results

6.1. Differential cross-sections

Using the method described in Section 5.1, we have been able to make DCS measurements for both Ar and Kr at energies ranging from 0.4 to 2.0 eV [27]. The DCS data presented here were taken using our earlier accumulator, which was not optimized for such measurements. Although the experimental setup and operation are similar to that described in Section 4, the details of the experiment are quite different and are described elsewhere [27]. Fig. 7 shows the raw data, taken on the new scattering apparatus designed specifically for such experiments. The data are normalized to unity for a 1 eV positron beam scattered from argon atoms. The open circles are the positron beam data with no argon gas present. The closed circles are the scattered positron beam where the pressure in the gas cell has been adjusted for approximately 10% total scattering. Because the positron beam energy (1 eV) is below all inelastic processes, such as positronium formation and electronic excitation, the scattering is purely elastic. The bottom axis of Fig. 7 shows the applied voltage on the RPA. The upper axis shows the corresponding scattering angle θ, as defined by Eq. (1), for a given loss in the positron's parallel energy. For example, a 1 eV positron which scatters transferring 0.2 eV into $E_\perp$, leaving 0.8 eV in $E_\parallel$, corresponds to a scattering angle of approximately 27°. Note that the upper axis shows only

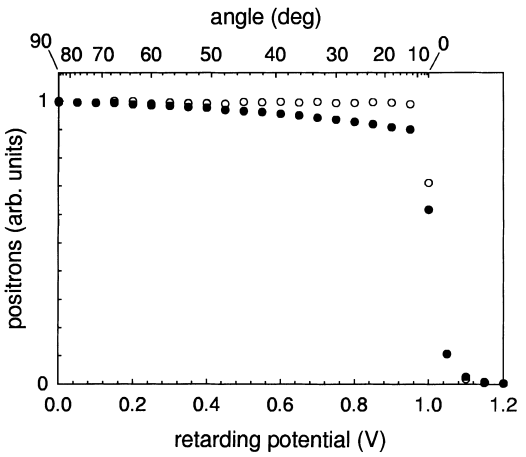

Fig. 7. RPA data for positron–argon elastic scattering: (○) 1 eV positron beam with no argon gas present; (●) positron beam after scattering from argon. The upper horizontal axis indicates scattering angle corresponding to a given positron parallel energy which is shown on the lower axis.

scattering angles up to 90°. Positrons that are scattered greater than 90°, (i.e. back-scattered) exit from the entrance of the gas cell. These back-scattering events are discussed in Section 7.

Fig. 8 shows absolute DCS measurements in atomic units for positron–krypton scattering at energies of 1.0 and 2.0 eV. Our experiment simultaneously collects both back-scattered and forward-scattered positrons (see Section 7), and so the DCS data are plotted versus the scattering angle, folded around $\theta = \pi/2$. We compare these data with the polarized orbital calculation by McEachran et al. [34], which has also been folded around $\theta = \pi/2$. There is good absolute agreement between the DCS data and theory over the entire range of energies and angles. For the energies of these measurements, the theoretical contribution due to back-scattering is negligible, so the data represent mainly the forward-scattered positrons.

For the data taken on our earlier apparatus (i.e., Figs. 8, 9 and 11), the dominant source of error is statistical fluctuations due to low repetition rates. This causes an uncertainty in the measurement of $\sim \pm 20\%$. As described in Section 4, our new scattering apparatus has a greatly improved repetition rate (2 s versus 20 s), which should improve this statistical error by $\sqrt{10}$ for a data set taken in the same amount of time. Another source of error, which is systematic in nature, is our ability to accurately measure the test-gas pressure. This pressure is measured using a stable ion gauge located outside the scattering cell. We extrapolate the pressure inside the cell using a

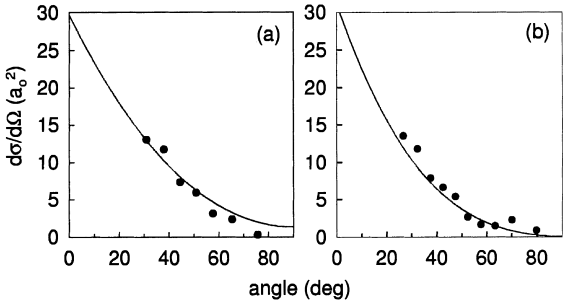

Fig. 8. Absolute differential elastic cross-sections for positron–krypton scattering at energies of (a) 1.0 and (b) 2.0 eV. Solid lines are theoretical predictions of McEachran et al. [34], folded around $\theta = \pi/2$ (see Section 7). There are no fitted parameters.

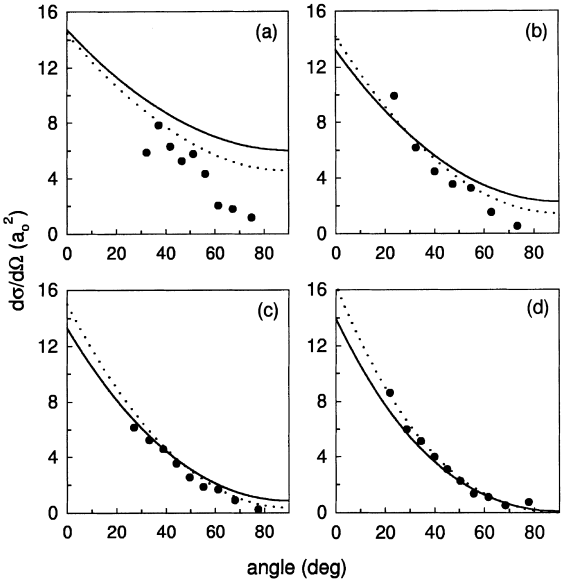

Fig. 9. Differential elastic cross-sections for positron–argon scattering at 0.4, 0.7, 1.0 and 1.5 eV are shown in plots (a)–(d), respectively. Solid and dotted lines are the theoretical predictions of McEachran et al. [36] and Dzuba et al. [37], respectively. The data and theory are folded around $\theta = \pi/2$ because the experiment does not distinguish between forward- and back-scattered positrons (see Section 7).

particle code simulation [35]. We believe that the combination of using the external ion gauge and the particle code provide an absolute pressure measurement better than 10%. In the new scattering apparatus, this systematic error has been reduced to less than 1% by directly measuring the test-gas pressure (see Section 4).

We also measured previously the DCS for positron scattering from argon, which has a total scattering cross-section roughly half that of krypton [27]. Fig. 9 shows the absolute DCS for positron–argon scattering at energies from 0.4 to 1.5 eV. The solid lines are the predictions of the polarized orbital calculations of McEachran et al. [36]. The dotted lines are the predictions of a many-body theory by Dzuba et al. [37]. For the larger beam energies, 1.0 and 1.5 eV, there is good agreement between the experiment and theory at all angles. However, at lower beam energies, 0.4 and 0.7 eV, there is a systematic disagreement between the data and predictions for large angles ($\theta \geqslant 60°$). We believe that this is due to the effect of trapped positrons making multiple passes through the scattering cell. A discussion of this effect and the method we have developed to circumvent it is discussed in Section 7.

6.2. Total inelastic cross-sections

Using the cold beam, we previously measured the first low-energy total vibrational cross-section for positron–molecule scattering, studying the excitation of the vibrational modes in CF_4 [27]. The data in Fig. 10, which were taken using our new scattering apparatus, show the integrated parallel energy distribution of positron–CF_4 scattering, with magnetic ratios (a) $M = 10$ and (b) $M = 1$ between the analyzer and scattering cell. The closed and open circles are measurements for a 0.55-eV positron beam with and without the CF_4 test-gas present. The arrows correspond to an energy loss of ≈ 0.16 eV due to the excitation of a vibrational mode in CF_4. We have identified this energy loss to be due to the asymmetric stretch mode v_3 (0.157 eV). This is the dominant mode observed in both electron scattering and infra-red absorption experiments [38,39], and it closely matches the energy loss that we observe. It is clear from Fig. 10 that the application of a magnetic ratio between the scattering cell and analyzer greatly reduces the effect of elastic scattering on $E_{\|}$, thus permitting accurate measurement of the inelastic scattering cross-section (see Section 5.2). The probability of an inelastic scattering event is determined from Fig. 10(b) by measuring the magnitude of the scattered component relative to that of the incident beam. The total vibrational cross-section is then calculated using the scale factor C in Eq. (4).

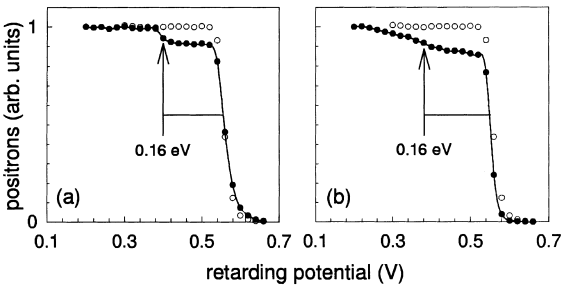

Fig. 10. RPA data for a positron–CF_4 inelastic scattering event with a magnetic ratio between the scattering cell and analyzer of $M = 10$ in (a) and $M = 1$ in (b). The open circles correspond to a 0.55 eV positron beam with no CF_4 present. The solid circles with a spline fit (solid line) correspond to the scattered beam following excitation of the dominant vibrational mode (v_3) in CF_4. The arrow indicates the 0.16 eV energy loss due to the vibrational excitation.

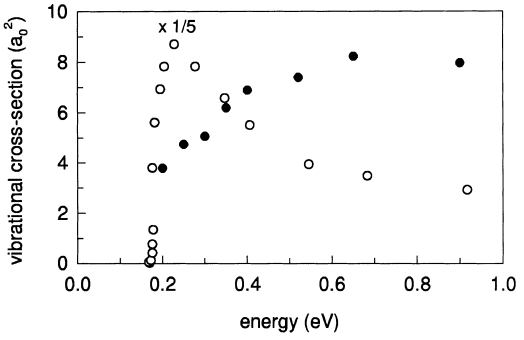

Fig. 11. Inelastic cross-section as a function of energy for the vibrational excitation of CF_4: (•) by positrons, and (○) from electron swarm data. The electron data are from [39] and plotted at 1/5 actual value. The collisions with CF_4 excite the asymmetric stretch mode v_3 at an energy of 0.157 eV.

Fig. 11 shows the inelastic cross-section as a function of beam energy for positron and electron collisions with CF_4. The data in Fig. 11 were taken using our earlier scattering apparatus, which has a maximum magnetic ratio $M = 3$. Although this ratio does increase the separation between elastic and inelastic scattering events, it is not large enough to completely remove all elastic effects from the parallel energy distribution, and this represents a source of systematic error in the measurements. We compare our data with the only available electron vibrational cross-section measurements for CF_4, which were obtained using the swarm technique [39]. While the electron cross-section has a distinct peak above the v_3 threshold (0.157 eV), the positron data are qualitatively different. This difference raises potentially interesting theoretical questions [8]. Although there is theoretical work on the excitation of vibrational modes in molecules by positrons [5,40,41], to our knowledge there are no theoretical predictions for positron scattering from CF_4. The only other measurements we are aware of for positron scattering from CF_4 are the total cross-sections measured above 1 eV by Sueoka [1].

7. Measurements using a magnetic beam – further considerations

While scattering experiments in a highly magnetized system have some unique advantages over experiments performed using an electrostatic beam, there are also disadvantages to this approach. One difficulty is the detection of back-scattered positrons. In an electrostatic experiment this is relatively easy as long as the experiment has the capability to move the detector beyond a 90° scattering angle, which is usually possible except near 180°. In our system, the positrons are forced to follow the magnetic field after scattering. Fig. 12(b) depicts the path of a positron as it back-scatters at 150° from an atom or molecule. The location of the positron accumulator, the scattering cell, and analyzer are shown in Fig. 12(a). The horizontal arrows show the path of the positron through the scattering apparatus, while the vertical arrows depict the energy transfer from $E_\parallel$ into $E_\perp$

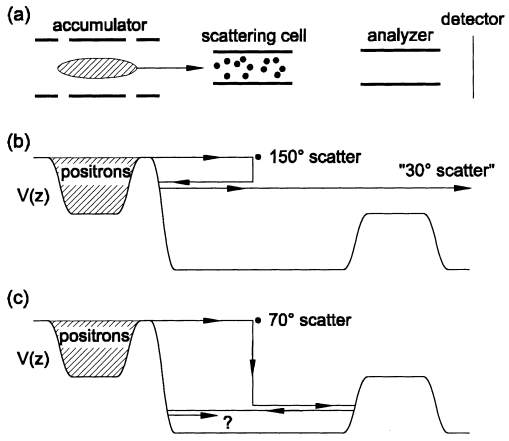

Fig. 12. (a) Schematic diagram of the scattering experiment, showing the relative positions of the positron accumulator, scattering cell and retarding potential analyzer. The lower figures show the path of a positron: (a) after a 150° scatter with the test-gas; (b) after a 70° scatter. Vertical parts of the trajectories indicate a transfer of energy from the parallel energy component $E_\parallel$, into the perpendicular component $E_\perp$, due to elastic scattering events.

due to an elastic scattering event. When the positron back-scatters, it transfers some of its parallel energy into perpendicular energy and travels back out of the entrance of the scattering cell. Since it has lost some $E_\parallel$, it is then reflected by the potential barrier created by the positron accumulator (see Fig. 12(b)) and travels back through the scattering cell, where it has a 90% probability of passing through the cell without scattering (since the single pass scattering probability has been adjusted to be 10%). If the positron is not scattered in the second pass through the cell, the RPA will detect the positron as if it were scattered at 30° in the forward direction. Thus, we are unable to distinguish between back-scattered and forward-scattered positrons, and so we display the DCS results as a superposition of the two scattering components folded around $\theta = \pi/2$. We are currently developing a technique to time-resolve the data which will allow us to distinguish between the back-scattering and forward-scattering events in order to obtain the full DCS.

Another effect of scattering in a magnetic field was discovered through a systematic discrepancy between our DCS data and theoretical predictions

for large angle scattering ($\theta > 60°$) (see Section 6.1). We noticed that when the theory predicted appreciable scattering cross-sections at large angles, our experimental results were consistently low (see Fig. 9(a) and (b)). Fig. 12(c) shows the motion of a positron as it scatters elastically at 70°. In this scattering event, the positron transfers an appreciable amount of $E_{\parallel}$ into $E_{\perp}$. If the RPA is set up to discriminate against a 70° scattering event, the scattered positron will be trapped in the potential well created by the analyzer and the positron accumulator exit gate, as shown in Fig. 12(c). After each bounce, the positron passes through the scattering cell potentially rescattering from the test-gas. If the positron rescatters, it can transfer some of its $E_{\perp}$ back into $E_{\parallel}$, thereby allowing it to pass through the analyzer and be detected. This will have the effect of making large angle scattering events look like small angle ones in the DCS data. Since the positron must bounce back and forth a number of times before it has a significant chance of rescattering, these secondary scatters can be eliminated by time-resolving the measurement.

Such time-resolved measurements have been accomplished using a potential barrier (not shown in Fig. 12(a)) located in front of the detector, to prevent any trapped positrons which have rescattered from reaching the detector. The potential barrier is raised after a few microseconds, which is enough time for the initial scattered beam to pass the barrier, but is still short enough to block any rescattered positrons. A typical bounce time for a trapped positron is a few microseconds, and so in order to distinguish between the initial scattering event and the rescattered positrons, the beam must have a pulse width less than this. We have been able to create cold pulsed positron beams with a FWHM pulse width less than 1 μs, which are suitable for this purpose. Fig. 13 shows the effects of time resolution on a 0.7 eV positron–argon DCS. The open circles and filled circles are data taken without and with time-resolution, respectively. Looking at the solid lines, which are fitted to the data, one can see that time-resolution in the DCS measurement results in an increase in the large angle scattering and a decrease in the small angle scattering, which is what one would expect if the rescattered positrons were eliminated. Thus the data in Fig. 13 indicate that, by time-resolving the data, we can eliminate the difficulty of secondary scattering at large angles.

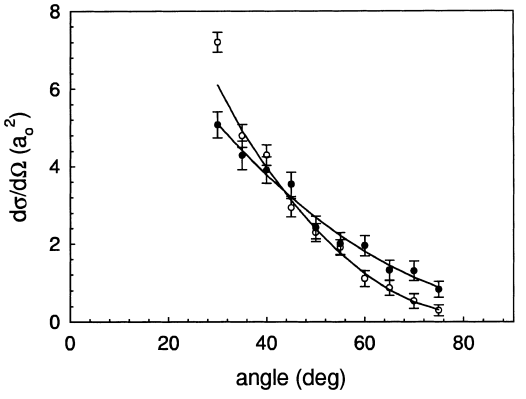

Fig. 13. Effects of time-resolving the DCS measurement for 0.7 eV positron–argon scattering: (○) data taken without time-resolution; (●) with time-resolution ($\Delta t = 6$ μs). The solid lines are fit to the data. Time-resolution increases the detection efficiency for large angle scattering events.

Another complication in studying scattering using a highly magnetized system is the insensitive detection of scattering events near 90°. Eq. (3) shows that the probability of a scattering event is proportional to the positron's path length. As we have discussed, a positron in a magnetic field travels along a helical path. Therefore, the path length of a positron traveling through the scattering cell will be greater than the length of the cell. The ratio of these two lengths depends only on the ratio of the energy components, $E_{\perp}$ and $E_{\parallel}$,

$$l_{\text{helix}}/l_{\parallel} = \sqrt{1 + E_{\perp}/E_{\parallel}}, \tag{7}$$

where l_{helix} is the path length of the positron and $l_{\parallel}$ is the effective path length for a positron moving in a straight line along the magnetic field. For a cold positron beam with $E_{\parallel}$ of 1 eV and $E_{\perp}$ of 0.025 eV, the ratio $l_{\text{helix}}/l_{\parallel}$ is 1.01, or a 1% correction to the straight path, which is negligible. Problems occur for scattering events close to 90°. In this case, the positron transfers nearly all of its parallel energy into the perpendicular component. It then moves slowly through the cell, gyrating rapidly in the direction perpendicular to the magnetic field until it makes another scattering collision. We can es-

timate the maximum angle at which single scattering can be assumed by requiring that the probability for a second scattering event is small. On average, the positron will scatter in the center of the gas cell. Since we have set the probability of scattering to 10% for a path length l equal to the scattering cell length, we can increase the path length by a factor of 6 and still have an acceptable probability for a second scatter of only 30%. Using Eqs. (1) and (7), this implies that any initial scattering at less than 80° will have less than a 30% chance of scattering a second time.

Some difficulties are common to both the magnetized and electrostatic scattering experiments. An example is the measurement of differential scattering near 0°. For the electrostatic case, the problem is caused by an inability to physically locate the detector near the unscattered beam, which is necessary to measure small-angle scattering. The difficulty for the magnetized system is the inability to separate the parallel energy distribution for small angle scattering from that of the incident beam. This difficulty is compounded by effects represented in Eq. (1), which relates the scattering angle to an energy transfer out of $E_{\parallel}$ and into $E_{\perp}$. One can see from this equation, which is plotted as the upper horizontal axis in Fig. 7, that scattering angles below 10° are difficult to study, even with our cold positron beam. This problem can, in principle, be circumvented using a colder beam. Similar problems to those near 0° are encountered for scattering angles near 180° in both the magnetic and electrostatic experiments.

Conducting the experiments in a magnetic field has some distinct advantages and disadvantages compared to electrostatic scattering experiments. The distinct advantage is that we can conveniently use our state-of-the-art cold positron beam. Besides that, advantages include a large effective detector size (all scattered positrons are collected), no moving parts, and a simple gas cell and analyzer design (with no need for a complicated gas jet). Some of the disadvantages include a more complicated analysis, differential cross-sections near 90° are difficult to detect, and measuring the DCS with both elastic and inelastic processes present is also difficult (see Section 7).

8. Concluding remarks

We have begun to exploit the ability to produce a state-of-the-art cold positron beam to study low-energy atomic and molecular physics. This effort has led us to investigate techniques to study scattering events in a magnetic field. We are continuing to improve our understanding of this type of experiment. Even at this early stage of development, we have been able to make new measurements in the energy range below 1 eV, including DCS measurements where even the equivalent electron experiments have proven difficult. As discussed above, we have been able to make the first measurements of low-energy positron–molecule vibrational cross-sections, studying positron–CF_4 collisions down to positron energies as low as 0.2 eV. We have also measured low-energy positron–atom elastic DCS for argon and krypton at energies ranging from 0.4 to 2.0 eV. We have every reason to believe that this ability to study low-energy positron matter interactions can be greatly expanded.

We hope to use information from these kinds of experiments to answer such open questions as the possible existence and nature of low-lying positron–molecule resonances and weakly bound states. For example, by measuring the DCS in the regime where $ka < 1$, where k is the momentum of the positron and a is the s-wave scattering length, it should be possible to use asymptotic formulae to measure the sign and magnitude of the scattering length, and thereby determine the expected energies of bound states or resonances [42]. We should also be able to study other low-energy scattering effects, such as Ramsauer–Townsend minima, and a detailed exploration of the vibrational excitation of molecules by positrons.

We are currently constructing a high field (5 T) ultra high vacuum positron accumulator [32]. In this device, the positron plasmas will be surrounded by electrodes cooled to 4 K, and so the plasma will equilibrate to this temperature by cyclotron radiation. The device will incorporate a rotating electric field to radially compress the plasma [43], thereby increasing the plasma density and the brightness of extracted positron beams. Using this accumulator as a reservoir of cold

positrons, in principle, it should be possible to produce extremely bright milli-electron-volt positron beams for use in a broad range of experiments.

We are also investigating possible techniques to measure the scattering cross-section, $\sigma(E_0, E, \theta)$ when both elastic and inelastic processes are present. Here, E_0 and E are the incident and scattered positron energies and θ is the scattering angle. This can in principal be accomplished by taking retarding-potential data sets at different magnetic ratios M, and using analysis techniques similar to tomographic reconstruction to unfold $\sigma(E, \theta)$ [44]. By continuing to push the limits of low-energy positron scattering, we hope to study a broad range of positron–matter interactions, not only in atomic and molecular systems but also in materials and at material surfaces [45].

Acknowledgements

We would like to thank Dr. Gleb Gribakin for many helpful discussions and E.A. Jerzewski for his expert technical assistance. This work is supported by National Science Foundation grant PHY 96-00407. The cold positron beam was developed with support from the Office of Naval Research, grant N00014-96-10579.

References

[1] W.E. Kauppila, T.S. Stein, Adv. At. Mol. Opt. Phys. 26 (1990) 1.
[2] O. Sueoka, A. Hamada, J. Phys. Soc. Jpn. 62 (1993) 2669.
[3] A. Hamada, O. Sueoka, J. Phys. B 27 (1994) 5055.
[4] G. Laricchia, M. Charlton, Philo. Trans. R. Soc. London, Ser. A 357 (1999) 2259.
[5] M. Kimura, M. Takeawa, Y. Itikawa, Phys. Rev. Lett. 80 (1998) 3936.
[6] K. Iwata, G. Gribakin, R.G. Greaves, C.M. Surko, Phys. Rev. A 61 (2000) 022719.
[7] K. Iwata, R.G. Greaves, T.J. Murphy, M.D. Tinkle, C.M. Surko, Phys. Rev. A 51 (1995) 473.
[8] G.F. Gribakin, Phys. Rev. A 61 (2000) 022720.
[9] S. Zhou, H. Li, W.E. Kauppila, C.K. Kwan, T.S. Stein, Phys. Rev. A 55 (1997) 361.
[10] P.J. Schultz, K.G. Lynn, Rev. Mod. Phys. 60 (1988) 701.
[11] A.P. Mills Jr., Exp. Methods Phys. Sci. 29A (1995) 39.
[12] A. Passner, C.M. Surko, M. Leventhal, A.P. Mills Jr., Phys. Rev. A 39 (1989) 3706.
[13] L.D. Hulett Jr., D.L. Donohue, J. Xu, T.A. Lewis, S.A. McLuckey, G.L. Glish, Chem. Phys. Lett. 216 (1993) 236.
[14] R.H. Howell, T.E. Cowan, J. Hartley, P. Sterne, B. Brown, Appl. Surf. Sci. 116 (1997) 7.
[15] M. Charlton, Rep. Prog. Phys. 48 (1985) 737.
[16] P.G. Coleman, J. McNutt, Phys. Rev. Lett. 42 (1979) 1130.
[17] M. Allan, J. Phys. B 28 (1995) 5163.
[18] B. Mojarrabi, R.J. Gulley, A.G. Middleton, D.C. Cartwright, P.J.O. Teubner, S.J. Buckman, M.J. Brunger, J. Phys. B 28 (1995) 487.
[19] S.L. Lunt, D. Field, S.V. Hoffman, R.J. Gulley, J.-P. Ziesel, J. Phys. B 32 (1999) 2707.
[20] A. Schramm, J.M. Weber, J. Kreil, D. Klar, M.W. Ruf, H. Hotop, Phys. Rev. Lett. 81 (1998) 778.
[21] J.C. Gibson, R.J. Gulley, J.P. Sullivan, S.J. Buckman, V. Chan, P.D. Burrow, J. Phys. B 29 (1996) 3177.
[22] M. Charlton, G. Laricchia, Hyperfine Interactions 76 (1993) 97.
[23] A.P. Mills Jr., E.M. Gullikson, Appl. Phys. Lett. 49 (1986) 1121.
[24] E.M. Gullikson, A.P. Mills Jr., W.S. Crane, B.L. Brown, Phys. Rev. B 32 (1985) 5484.
[25] S.J. Gilbert, C. Kurz, R.G. Greaves, C.M. Surko, Appl. Phys. Lett. 70 (1997) 1944.
[26] C. Kurz, S.J. Gilbert, R.G. Greaves, C.M. Surko, Nucl. Instr. and Meth. Phys. B 143 (1998) 188.
[27] S.J. Gilbert, R.G. Greaves, C.M. Surko, Phys. Rev. Lett. 82 (1999) 5032.
[28] D. Segers, J. Paridaens, M. Dorikens, L. Dorikens-Vanpraet, Nucl. Instr. and Meth. A 337 (1994) 246.
[29] R. Khatri, K.G. Lynn, A.P. Mills Jr., L.O. Roellig, Mater. Sci. Forum 105–110 (1992) 1915.
[30] R. Suzuki, Y. Kobayashi, T. Mikado, H. Ohgaki, M. Chiwaki, T. Yamazaki, Hyperfine Interactions 84 (1994) 345.
[31] C.M. Surko, M. Leventhal, A. Passner, Phys. Rev. Lett. 62 (1989) 901.
[32] C.M. Surko, R.G. Greaves, K. Iwata, S.J. Gilbert, Nucl. Instr. and Meth. B 171 (2000) 2.
[33] R.G. Greaves, M.D. Tinkle, C.M. Surko, Phys. Plasmas 1 (1994) 1439.
[34] R.P. McEachran, A.D. Stauffer, L.E.M. Campbell, J. Phys. B 13 (1980) 1281.
[35] T.J. Bartel, S. Plimpton, J. Johannes, J. Payne, Icarus: A 2D Direct Simulation Monte Carlo (DSMC) Code for Parallel Computers, Users Manual – V3.0, Sandia National Laboratories Report SAND96-0591, 1996.
[36] R.P. McEachran, A.G. Ryman, A.D. Stauffer, J. Phys. B 12 (1979) 1031.
[37] V.A. Dzuba, V.V. Flambaum, G.F. Gribakin, W.A. King, J. Phys. B 29 (1996) 3151.
[38] A. Mann, F. Linder, J. Phys. B 25 (1992) 533.
[39] L.G. Christophorou, J.K. Olthoff, M.V.V.S. Rao, J. Phys. Chem. Ref. Data 25 (1996) 1341.
[40] G. Danby, J. Tennyson, J. Phys. B 24 (1991) 3517.

[41] F.A. Gianturco, T. Mukherjee, J. Phys. B 30 (1997) 3567.
[42] G.F. Gribakin, 1999, Private communication.
[43] F. Anderegg, E.M. Hollmann, C.F. Driscoll, Phys. Rev. Lett. 81 (1998) 4875.
[44] D. Boyd, W. Carr, R. Jones, M. Seidl, Phys. Lett. 45A (1973) 421.
[45] R.G. Greaves, C.M. Surko, in: J. Bollinger, R. Spencer, R. Davidson (Eds.), Nonneutral Plasma Physics III, AIP Conference Proceedings, Vol. 498, 1999, p. 19.